



CHORUS

This is the accepted manuscript made available via CHORUS. The article has been published as:

Intrinsic defects in multiferroic BiFeO_3 and their effect on magnetism

Tula R. Paudel, Sitaram S. Jaswal, and Evgeny Y. Tsybal

Phys. Rev. B **85**, 104409 — Published 14 March 2012

DOI: [10.1103/PhysRevB.85.104409](https://doi.org/10.1103/PhysRevB.85.104409)

Intrinsic defects in multiferroic BiFeO₃ and their effect on magnetism

Tula R. Paudel, Sitaram S. Jaswal and Evgeny Y. Tsymbal

Department of Physics and Astronomy, Nebraska Center for Materials and Nanoscience,
University of Nebraska, Lincoln, Nebraska, 68588

ABSTRACT

We investigate energetics of the intrinsic defects in bulk multiferroic BiFeO₃ and explore their implication for magnetization using a first-principles approach based on density functional theory. We find that dominant defects in oxidizing (oxygen-rich) conditions are Bi and Fe vacancies and in reducing (oxygen-poor) conditions are O and Bi vacancies. The calculated carrier concentration shows that the BiFeO₃ grown in oxidizing conditions has p-type conductivity. The conductivity decreases with oxygen partial pressure and the material becomes insulating with tendency for n-type conductivity. We find that the Bi and Fe vacancies produce a magnetic moment of about $1\mu_B$ and $5\mu_B$ per vacancy, respectively, for p-type BiFeO₃ and none for insulating BiFeO₃. O vacancies do not introduce any moment for both p-type and insulating BiFeO₃. Calculated magnetic moments due to intrinsic defects are consistent with those reported experimentally for the bulk BiFeO₃.

I. INTRODUCTION

Multiferroic materials that simultaneously display magnetic and electric order have recently attracted significant interest due to their interesting physical properties promising for multifunctional device applications [1–13]. The magnetoelectric coupling between the electric and magnetic degrees of freedom where an electric (magnetic) polarization can be induced by a magnetic (electric) field is especially exciting [14,15]. Magnetoelectric multiferroics allow the possibility of switching the magnetization with electric field, which offers an ample opportunity for information storage applications [16,17].

BiFeO_3 (BFO) is a particular example of a single-phase multiferroic material that has recently attracted special attention due to its room temperature multiferroic properties [3,18,19]. Bulk BFO is antiferromagnetic with the Néel temperature $T_N=643\text{K}$ [20] and ferroelectric with the Curie temperature $T_C=1103\text{K}$ [21]. Theoretically predicted spontaneous polarization $P_s \sim 100 - 150 \mu\text{C}/\text{cm}^2$ [22–24] has been found in thin films at room temperature [3,18,25]. Bulk BFO, however, exhibits relatively low polarization $P_s \sim 5-10 \mu\text{C}/\text{cm}^2$ [26–28]. Bulk BFO has the rhombohedrally distorted perovskite[29] structure in which ionic sublattices are displaced relative to each other along the polar [111] direction, and the oxygen octahedra are rotated around the same [111] axis [22]. When grown as a thin film BFO may have monoclinic (BB or BB') or tetragonal (P4mm) structure depending upon the strain imposed by underline substrate. For example, at room temperature a BFO film grown on a highly mismatched LaAlO_3 substrate has P4mm structure [30,31], on SrRuO_3 (SRO)/ SrTiO_3 (STO) it is monoclinic [32] and on LaNiO_3 (LNO) it has a mixed phase of R3c and P4mm [33]. At higher temperature ($\sim 700\text{K}$)

both the bulk single crystal and a thin film sample undergoes a structural phase transition to the orthorhombic and eventually ($\sim 1100\text{K}$) to the cubic perovskite [32].

Bulk BFO exhibits a G-type antiferromagnetic order[34], where the magnetic moment of each Fe cation is antiparallel to that of its nearest neighbors. The calculated magnetocrystalline anisotropy predicts that a preferred orientation of the Fe magnetic moments is perpendicular to the polar [111] direction [35]. A small canting of the Fe magnetic moments leads to a net magnetization of about 5 emu/cm^3 . However, it was found that some thin films exhibit a very large saturation magnetization exceeding 70 emu/cm^3 [36]. The origin of this large magnetization remains unclear.

Intrinsic point defects, especially oxygen vacancies (V_{O}), have been proposed as a possible source of the magnetization in BFO [36]. However, a comprehensive theoretical study to explore various possible point defects in BFO and their effect on magnetization is still lacking. Ju and Cai studied the electronic structure of oxygen vacancies and its effect on the dielectric properties of the BFO [37]. Clark and Robertson studied their ionization energy [38]. Zhang *et al.* investigated energies of formation of the oxygen and cation vacancies and discussed their possible implications for the conductivity of BFO [39]. All the above reports did not consider the effects of individual point defects on the net magnetization of BFO. Ederer and Spaldin investigated the effect of oxygen vacancies on weak ferromagnetism of BFO [35]. They found that oxygen vacancies lead to the formation of Fe^{2+} and can slightly alter the magnetization.

In this paper, using a first-principles approach based on density functional theory, we explicitly calculate the energetics of possible intrinsic point defects in bulk BFO, i.e., cation and anion vacancies as well as anti-site defects. There are no high symmetry vacant interstitial sites and hence such defects are not considered. As all defects are treated on the same footing, we can quantitatively compare the tendency of formation of various defects and their effects on properties of BFO. We find that dominant defects in oxidizing conditions are Bi and Fe vacancies and in reducing conditions are O and Bi vacancies. The calculated carrier concentration shows that the BFO grown in oxidizing conditions has p-type conductivity. The conductivity decreases with oxygen partial pressure and the material becomes insulating with tendency for n-type conductivity. We find that the Bi and Fe vacancies produce a magnetic moment of about $1\mu_B$ and $5\mu_B$ per vacancy, respectively, for p-type BFO and none for insulating BFO. O vacancies do not introduce any moment for both p-type and insulating BFO. Calculated net magnetizations due to intrinsic defects are consistent with those that reported experimentally for the bulk BFO[40,41].

The rest of the paper is organized as follows. First, we briefly describe our computational approach. Then, we consider conditions for thermodynamic stability of the BFO compound based on the range of chemical potentials for constituent elements. Next we discuss the formation of various point defects and their electronic structure. Then we address a possible modification to the BFO magnetization due to coupling between the defects and the host magnetic Fe ion. Finally, we discuss the effect of the defects on the net magnetization of BFO and conclude the article.

II. COMPUTATIONAL METHODS

We use density functional theory (DFT) band structure approach as implemented in Vienna *ab initio* simulation package (VASP) [42,43]. The projected augmented wave (PAW) method is used to approximate the electron-ion potential [44]. To treat exchange and correlation effects we use both the local density approximation (LDA) [45] and the semi-empirical LDA+U method [46] within a rotationally invariant formalism [47], for a better description of the localized transition metal *d* electrons. Here we choose $(U-J) = 3\text{eV}$ for the *3d* orbitals of Fe atoms, as this value of U provides good thermodynamics for a wide range of binary and ternary oxides [48] including Fe-oxides and it provides a reasonable magnetic structure [49].

We construct an 80 atoms supercell by doubling a R3c all three lattice vectors. G type anti-ferromagnetic order of the original cell is maintained. Vacancy is created by removing an atom in the supercell. Similarly, an anti-site defect (Fe_{Bi} and Bi_{Fe}) is created by substituting an atom of one type by another. Then, we relax the ions in the supercell keeping its shape fixed until the Hellman-Feynman forces are less than $0.01\text{eV}/\text{\AA}$. In the calculation, we use a kinetic energy cutoff of 340 eV for the plane wave expansion of the PAWs[44] and $2\times 2\times 2$ Monkhorst-Pack grid of k points [50] for Brillouin zone integration. In all calculations, we turn on the spin polarization and switch off all symmetries other than time reversal to allow for possible symmetry broken relaxation around the defect. We do not include the spin-orbit interaction in our calculations. The spin-orbit interaction results in the energy corrections, which are of the order of micro- to milli-eV, whereas the energies that we are dealing with here are of the order of eV. It is known that the spin-orbit interaction in conjunction with the exchange coupling leads to the Dzyaloshinskii-Moriya interaction which is responsible for a weak ferromagnetism in some oxide materials

including BFO, where magnetization of 0.1 $\mu\text{B}/\text{unit cell}$ [49] has been reported associated with this effect. Here, we neglect this contribution.

Various non-isovalent defects have different ionization levels. For example, V_{Bi} and V_{Fe} have three ionization levels and V_{O} has two ionization levels. To create an ionized (charged) defect, we add or remove electrons to the system and include a compensating jellium background.

Additional charge in the system introduces two complications. The first is the interaction between the charge and its image. We take this into account by adding to the total energy the screened Madelung energy of the point charge-image interaction in a lattice compensated by jellium background, as suggested by Leslie and Gillan [51], and the screened interaction between the delocalized part of the charge and its image due to Makov and Payne [52]. The dielectric constant that determines screening is calculated using density functional perturbation theory [53] as implemented in VASP. The second complication is the arbitrary shift in the total energy due to additional charge in the system. We correct this shift by calculating a difference in the atomic-sphere averaged electrostatic potentials between the host and charged system [54]. These corrections effectively remove the supercell size dependent energy of a charged system [54,55] and effectively represent the energy of an infinite crystal with a single charge (dilute limit). This approach has been used in various oxides system [56–60] including spinels [61] to calculate the formation enthalpy (ΔH_f) of the (charged) defect in dilute limit.

The formation enthalpy of various defects in the system can be used to calculate their concentration at a given temperature in the dilute limit even if the supercell size used in the first-principles calculation is smaller to accommodate such dilute concentrations. We describe this

approach in sec III-C. In brief, we minimize the Gibbs free energy of a system with various defects as a function of the defect concentration. We then self consistently find the defect concentration (C_D), the Fermi energy (E_F^{eq}), and the carrier concentration as functions of temperature.

III. RESULTS

A. Range of chemical potentials and stability of BiFeO₃

The enthalpy of formation of BFO is defined with respect elements at ambient conditions as $H_f = E(BFO) - \mu_{Bi}^{el} - \mu_{Fe}^{el} - 3\mu_{O}^{el}$. However, solid BFO usually is the product of the high temperature reaction between Fe₂O₃ and Bi₂O₃. Chemical potentials (μ) of Bi, Fe and O elements in such a reaction are different from those of elemental Bi, Fe and O (μ^{el}) by an amount $\Delta\mu$ such that $\mu = \mu^{el} + \Delta\mu$. There exists a certain region of chemical potentials, where a pure BFO exists. This region is determined by the following conditions: $\Delta\mu_{Bi} + \Delta\mu_{Fe} + 3\Delta\mu_{O} \geq \Delta H_f(BFO)$, $2\Delta\mu_{Fe} + 3\Delta\mu_{O} \leq \Delta H_f(Fe_2O_3)$, and $2\Delta\mu_{Bi} + 3\Delta\mu_{O} \leq \Delta H_f(Bi_2O_3)$, where for convenience we set $\mu^{el} = 0$. The values of H_f for competing phases Bi₂O₃ and Fe₂O₃, here are taken from tabulated experimental values [62]. Solving these three relations, we can eliminate $\Delta\mu_{O}$ and express the chemical potential of one of the cations in terms of the other (i.e., $\Delta\mu_{Fe}$ in terms of $\Delta\mu_{Bi}$) to determine the diagram of stability. Using the correct values of H_f is crucial as they directly affect the range of chemical potentials where BFO is stable. Since H_f of competing phases are taken from experiments and atomic chemical potentials are fitted to produce such values, room for uncertainty in calculated ranges of the chemical potentials is very small, including an error in calculating the total energy of BiFeO₃. Fig. 1 shows the stability regions of different compounds

against Bi and Fe chemical potentials. The black and blue lines in this figure represent the stability transition lines between Fe_2O_3 and BFO and Bi_2O_3 and BFO respectively. The stability region of BFO is indicated in the green. It is seen from Fig. 1 that $\Delta H_f(\text{BFO})/2 \leq \Delta\mu_{\text{Fe}}$ and $\Delta\mu_{\text{Bi}} \leq 0$, and $-2.0 \text{ eV} \leq \Delta\mu_{\text{O}} \leq 0$. In the oxidizing (oxygen rich) conditions ($\Delta\mu_{\text{O}} \approx 0$), $\Delta\mu_{\text{Fe}}$ and $\Delta\mu_{\text{Bi}}$ are large-negative and represent the metal poor conditions, whereas in the reducing (oxygen poor) conditions ($\Delta\mu_{\text{O}} \sim -2 \text{ eV}$), $\Delta\mu_{\text{Fe}}$ and $\Delta\mu_{\text{Bi}}$ are either zero or small negative (see Fig. 1) and represent metal rich conditions.

Enthalpies of formation of competing phases such as Bi_2O_3 , Fe_2O_3 , Fe_3O_4 , FeO , $\text{Fe}_4\text{Bi}_2\text{O}_9$, $\text{Bi}_4\text{Fe}_2\text{O}_9$ as well as O_2 molecules were calculated. The chemical potential of the [oxygen molecule](#) includes the corrections suggested in Ref.[59] that take into account a zero point energy as well as the extra contribution required to fit the calculated heats of formation to the large data set of oxides[48]. The chemical potential of elemental Bi is calculated by fitting to the experimental heat of formation of Bi_2O_3 [62]. The chemical potential of elemental Fe is the average chemical potential obtained by fitting to the experimental heat of formation of the FeO , Fe_2O_3 and Fe_3O_4 [62].

Elemental chemical potentials of Fe and Bi represent the total energy of elemental solids and chemical potential of oxygen represents the energy of half the oxygen molecule. The formation energy calculations require the chemical potentials of the constituent elements of the compound. In LDA+U calculations, the same values of U for Fe in metallic phase and Fe in BFO are not expected to be very realistic [59]. We find that using the elemental chemical potentials obtained by fitting to the heat of formation of competing phases provide the calculated heat of formation

of BFO consistent with the experimental result [63]. Since the elemental chemical potentials are fitted to produce the heat of formations of the binary oxides, the relative stability of the competing phases is also correct. The stability of competing phases directly affects the range of the chemical potentials for which the compound of interest is stable.

In BFO the calculated range of stability is narrow (the green area in Fig. 1); signifying the heat of reaction between the Bi_2O_3 and Fe_2O_3 is small and the compound is border line. Nevertheless there are no other phases that limit the formation of the BFO in very oxidizing conditions. However the small enthalpy of formation (-7.4 eV) of BFO limits its formation in very reducing conditions. As a result the range of oxygen chemical potential that BFO is stable is relatively narrow (-2.0 eV $\leq \Delta\mu_{\text{O}} \leq 0$) compared to other perovskites such as STO (-5.7 eV $\leq \Delta\mu_{\text{O}} \leq 0$) or LAO (-6.0 eV $\leq \Delta\mu_{\text{O}} \leq 0$). The existence of other phases, such as Fe_3O_4 , $\text{Bi}_2\text{Fe}_4\text{O}_9$, and $\text{Fe}_2\text{Bi}_4\text{O}_9$, was found not to affect the stability of BFO.

The calculated oxygen chemical potential translated into the set of temperature and pressure by using ideal gas as, $\Delta\mu_{\text{O}}(T, P) = (H_0 + c_p(T - T_0) - TS_0 + Tc_p \ln(T/T_0) + k_B T \ln(P/P_0))/2$ with $c_p = 3.5k_b$, where $k_b = 1.4 \times 10^{-23}$ m²kg s⁻²K⁻¹ and tabulated values of oxygen at $T_0 = 298$ K and $P_0 = 1$ atm are $H_0 = 8700$ Jmol⁻¹ and $S_0 = 205$ Jmol⁻¹K⁻¹ [62], are indicated in Fig. 1 by the dashed lines. The $\Delta\mu_{\text{O}} = 0$ is virtually unachievable as it corresponds to 2000°C temperature and 120 atm pressure.

B. Formation and ionization of intrinsic point defects

Energy of formation of a defect D is the energy cost to add (remove) an atom of charge q to (from) otherwise perfect host. Assuming thermal equilibrium between the host and charge

interchanging reservoirs that are characterized by chemical potentials μ_{removed} and μ_{added} for removed and added atoms respectively, the energy of defect formation is defined by $\Delta H_f(D,q) = E(D,q) - E_H + \mu_{\text{removed}} + \mu_{\text{added}} + qE_F$, where $E(D,q)$ is the energy of the host with the defect, E_H is energy without defect, and E_F is the electrochemical potential of the charge q . E_F is usually measured with respect to the host valence band maximum (E_V).

Charge transition energy between two charge states q and q' of a defect represents the energy required to ionize a defect in the charge state q to the other charge state q' . This energy per unit charge is defined as $E(q/q') = (\Delta H_f(q) - \Delta H_f(q'))/(q' - q)$. Note that this transition energy is independent of the chemical potentials (growth conditions) due to their cancelation. Shallow donors with the transition levels closer to the conduction band minimum (CBM) and shallow acceptors with those closer to the valence band maximum (VBM) are easy to ionize and contribute to the overall conductivity in the compound. Deep defects have transition energies deep in the band gap. Such defects primarily behave as traps for the carriers.

Using the LDA+U method with $U - J = 3.0$ eV on the Fe-3d orbital we find the band gap of BFO to be about 1.7 eV. This value is about 1 eV lower than the direct optical band gap of 2.74 eV measured experimentally [63]. Therefore, in our thermodynamic calculations that are used to determine defect concentration we assumed a rigid shift of 1 eV to the conduction band. We expect that this shift would affect the behavior of shallow donor defects. Here only V_O donor level is deep with respect to the CBM. The upward shift of the conduction band further deepens already deep V_O level, however its effect on the number of defects as well as the conductivity remains unchanged.

Fig. 2 shows the formation energy of the most stable charge state of a defect as a function of the Fermi energy for one of the oxidizing and the most reducing conditions. In the oxidizing conditions, formation enthalpy of cation vacancies is smaller than 1.1 eV. At the maximum possible oxidizing condition $\Delta\mu_{\text{O}} = 0$ eV, $\Delta H_{\text{f}}(\text{V}_{\text{Bi}})$ drops to ~ 0.2 eV, whereas $\Delta H_{\text{f}}(\text{V}_{\text{O}})$ increases to ~ 2.0 eV. Enthalpy of formation of V_{Fe} is slightly larger than that of V_{Bi} , however follows the similar trend. This indicates cation vacancies to be the dominant defects in oxidizing conditions. This is consistent with the fact that in the oxidizing conditions V_{O} are unlikely to form, whereas V_{Bi} is likely to form, as Bi is known to be relatively volatile [64]. However, this contrasts to the relatively large energy of formation for cation vacancy reported in Ref. [39]. The difference comes mainly due to use of the different atomic chemical potentials for Fe and Bi. Enthalpy of formation of oxygen vacancy is also different; however, the difference is much smaller than that for cation vacancy. The small difference again comes from use of different chemical potentials of oxygen. We include a correction in the oxygen chemical potential that in part comes from fitting it to a large set of oxides enthalpy of formation and in part due to zero point motion. These different values also affect the range of chemical potentials and contribute to the differences mainly in reducing conditions. Further, cation defects have small transition energies and therefore are easily ionized and produce holes rendering compound p-type. This is consistent with that in Ref [39] as ionization energy is the energy difference between two charge states of the defects leaving behind the effects of chemical potentials at a given Fermi energy.

Equilibrium Fermi energy (E_{F}^{eq}) in the system is determined by charge neutrality condition. This can be achieved either by having equivalent number of free electrons and holes or having free holes (electrons) and their traps. Deep localized defects such as oxygen vacancy (in BFO) trap the carriers (holes). Oxygen vacancies dominate over the cation vacancies only when the Fermi

energy is shifted down toward the VBM, which may be achieved by doping with an external acceptor-type impurity, i.e. a dopant that creates holes in BFO. In this case the E_F^{eq} of the defect-rich BFO can be even pushed further below the VBM of the perfect BFO (down to -0.5 eV), as there is no defect that blocks the movement of the Fermi level. Note that the ideal oxidizing condition of $\Delta\mu_{\text{O}} = 0$, corresponding to BFO/O₂ equilibrium, is physically unrealistic. Hence we choose the oxidizing condition to be $\Delta\mu_{\text{O}} = -0.5$ eV, which is achievable in experiment using variety of temperatures and pressures, e.g. T=500°C and P=1atm. According to ideal gas law the oxygen chemical potential is a function of temperature and pressure (see Sec. III(A). One can fix temperature and vary pressure and vice versa to achieve the same chemical potential). Further at such temperature as 500°C, the thermal equilibrium between constituent ions in BFO can be expected even at the ambient pressure. To achieve $\Delta\mu_{\text{O}} = 0$ eV at ambient pressure one need to decrease temperature to 10 K. At such temperature no-reaction occurs, let alone the thermal equilibrium.

In the *reducing conditions*, the energy of formation is so high that both anion and cation vacancies are difficult to form. When under electron doping the Fermi level is pushed toward the CBM, the formation energy of the cation vacancy tends to decrease. The number of acceptor defects increases releasing holes and compensating the effect of doping that makes the compound insulating. However, the movement of the Fermi level is limited to a narrow range of 1.25 eV (shown by the shaded region in Fig. 2) around E_F^{eq} , much narrower than the band gap of 2.7 eV. When the Fermi level is moved beyond this range the compound becomes unstable due to spontaneous formation of large number of defects. For example, at O-poor conditions (Fig.2(b)), when the Fermi level falls down to 0.1 eV, oxygen vacancies start forming

spontaneously, and when it rises above 1.4 eV Bi vacancies start forming spontaneously, both destabilizing BFO.

The energy of formation of a defect depends partly on the local bonding environment. In BFO, since the Fe-O bond length of 1.93 Å is shorter than the Bi-O bond length of 2.31 Å, the formation of the Bi vacancy is easier than the formation of the Fe vacancy. This is consistent with our observation that $\Delta H_f(V_{Fe})$ is higher than $\Delta H_f(V_{Bi})$. Further anti-site defects are unlikely due to a large difference in their radii (Bi³⁺ ionic radius of 1.17 Å is about 32% larger than that of the Fe³⁺ ionic radius), consistent with the large heat of formation of the anti-site defects. We find similar behavior of point defects in other perovskites such as LAO, STO and BTO *viz.* vacancies have lower formation energy compared to the anti-site defects. However V_O can be formed in LAO, STO and BTO under much larger reducing conditions [as they can exist in more reducing conditions](#) ($\Delta\mu_O < -5$ eV) compared to BFO ($\Delta\mu_O \sim -2$ eV). Consequently calculated V_O formation energy is much higher in BFO compared to that in other perovskites including LAO (~0.4 eV), STO (~0.1 eV) or BTO (~0.1 eV).

C. Defect concentrations and oxygen chemical potentials

We calculate the number of defects $C_D(T, \mu_{O_2})$ by minimizing the Gibbs free energy. The latter is given by $G(D) = \Delta H_f(D) - TS$, with S being the entropy due to different ways of arranging the defects among the available sites (N), such that $C_D = N \exp[-\Delta H_f(D)/k_B T]$. Note that $\Delta H_f(D)$ depends upon growth conditions (μ_O) and the Fermi energy (E_F), where E_F depends on the number of carriers, some of which are coming from ionized defects. We then self consistently calculate E_F^{eq} and C_D at a given temperature [65] assuming an overall charge neutrality.

Obviously, the defect concentration increases exponentially with temperature. Instead, it is much more interesting to compare the defect concentration calculated at different $\Delta\mu_O$, as it effectively characterizes the number of defects in a sample grown under different growth conditions. In Fig. 3, we plot the number of defects as a function of the oxygen chemical potential at a given temperature. Again, $\Delta\mu_O = 0$ represents most possible oxidizing condition and increasingly negative $\Delta\mu_O$ represents various reducing conditions. It is seen from Fig.3 that the overall number of defects decreases in reducing conditions and the dominant defect changes from cation vacancies in the oxidizing conditions to the oxygen and Fe vacancies in the reducing conditions. Considering the fact that cation vacancies are shallow and hence a hole producer and oxygen vacancies are deep and act merely as a hole trap, the BFO compound, especially when grown under oxidizing conditions behaves as a p-type conductor as seen experimentally [66]. Conductivity of BFO decreases in reducing conditions, where it essentially behaves as an insulator. This behavior is typical of p-type oxides mainly due to the reason that the hole producer defects such as cation vacancies are easier to form and at the same time hole killer defects such as oxygen vacancies are less easy to form in oxidizing conditions. The large number of cation vacancies in this case does not necessarily mean a large hole conductivity as one can expect a very low hole mobility owing to the essentially flat valence band formed from the relatively localized Fe-3d band. Overall, our calculation indicates that the sample grown in oxidizing conditions is expected to be more conductive due to cation vacancies than the sample grown in reducing conditions. This prediction is consistent with the results of Ref. [67], where samples annealed in oxygen are found having larger conductivity than samples annealed in vacuum.

D. Electronic structure of point defects and their effect on the magnetization

1. Cation vacancies

Bi vacancies introduce three holes in the system with the possibility of carrier-induced ferromagnetism. The point group symmetry of the Bi in BFO is C_{3v} despite the fact that Bi is bonded with six oxygen atoms. One set of three Bi-O bonds have a bond length of 2.31 Å and another set of three Bi-O bonds have a bond length of 2.41 Å. In this symmetry, the dangling bond related state splits into $a^2e_g^4$ (super script represents the occupation of the level including spin polarization). Due to relaxation, when symmetry is lowered to C_1 , the e-like state splits into two a-like states, as seen from Fig. 4(a). In literature Bi has been sometimes treated as having approximate O_h symmetry reflecting small difference between two sets of Bi-O bonds. In terms of O_h symmetry, the dangling bond related state splits according to $a^2t_{2g}^6e_g^4$. Due to relaxation, the e-like state splits into two a-like states and analysis becomes the same as in the case of the C_{3v} point group symmetry.

In case of the charge neutral Bi vacancy, the lower a-like state is half filled whereas the upper a-like state is empty, and the Fermi level passes through the middle of the lower a-like state. The electron in the lower a-like state couples with one of the 3d-electrons in Fe with the spin in the same direction, producing a net magnetization of $1\mu_B$ per vacancy. In Fig. 4(b), we show this orbital and the possible coupling mechanism between the Bi vacancy and Fe.

In case of Bi vacancy in the 1^- charge state, the lower a_1 like state is filled with two spin-up and spin-down electrons resulting in no net magnetization. In the 2^- charge state, the upper a_1 like

state has one electron resulting in the magnetic moment of $1\mu_B$ /vacancy. In the 3^- charge state, the upper a_1 like state has two spin-up and spin-down electrons resulting in no magnetic moment. We emphasize, however, that the charge neutral V_{Bi} is dominant due to the p-type nature of the compound and thus no net magnetization in BFO is expected in this case.

In case of Fe vacancy, removing a Fe atom results in the net magnetization of about $5\mu_B$ per vacancy originating from the difference in magnetic moments between the two adjacent planes with the G-type anti-ferromagnetic arrangement of spins.

2. Oxygen vacancies

The charge neutral O vacancy leaves behind two uncompensated electrons in the system. Strictly speaking the oxygen point group symmetry in BFO is C_1 . In this symmetry, the a-like dangling bond related state lies in the gap, as seen from Fig. 5(a). (Note two unoccupied states in the gap). Another way to consider this is to start from oxygen having approximate T_d symmetry, in which the dangling bond related state splits into $a^2t_{2g}^6$ states. Lowering symmetry to C_{2v} leads to the t_{2g}^6 state splitting into a^2 and e_g^4 states. Additional lowering symmetry around the vacancy site to C_1 further splits the e_g -like orbital into two a-like orbitals. Out of these two the lower one lies in the valence band and the higher one lies in the band gap with two spin-up and spin-down electrons. Spin-up electron couples with spin-up Fe electron and spin-down electron couples with spin-down Fe electron resulting in the same change in either spin channel, and hence no net magnetization appears in the compound, as shown in Fig. 5 (b). In the 1^+ charge state, V_O carries moment of $1\mu_B$, but this state is unstable; while in the 2^+ charge state, V_O does not carry a significant moment.

3. Anti-site defects

Anti-site substitutions of Fe on Bi and Bi on Fe introduce a magnetic moment of $5\mu_B$ per defect as they create imbalance of the spin moment in the plane with respect to the adjacent plane in the G-type antiferromagnetic lattice of BFO. In reality, such defects can be expected to distribute randomly in either planes canceling moments each other's moment resulting no net magnetization.

4. Net magnetization

We define the net magnetization as $M = \sum_d C(d) m(d)$, where $C(d)$ is the concentration of defects and $m(d)$ is the magnetic moment per defect. When we introduce two Bi vacancies in our supercell calculation, the case where the net magnetic moment of the system doubles is found to be more stable, signaling that the moments due to V_{Bi} align ferromagnetically. Note that defect concentration used for the determination of ferromagnetic coupling is larger than that predicted by the enthalpy of formation. Similarly, for Fe vacancies two defects in a ferromagnetic layer create the net moment, which is equivalent to twice the local moment of one Fe atom. However, we find that two Fe vacancies lying in two antiferromagnetically aligned planes produce no net magnetic moment. Thus, assuming that Fe vacancies are randomly distributed leads to virtually no net magnetization in the bulk BFO. As we have already discussed, oxygen vacancies in the charge neutral state also do not produce any moment.

Using the number of defects shown in Fig. 3 and the magnetic moment they introduce in the system, we can calculate the net magnetization of bulk BFO. The result is as follows: ~ 2 emu/g

($0.0016 \mu_B/\text{f.u.}$, $0.25 \text{ emu}/\text{cm}^3$) at oxidizing conditions ($\Delta\mu_{\text{O}_2} = -0.2 \text{ eV}$). Here, we used the density of BFO to be $8.34 \text{ g}/\text{cm}^3$. This very small magnetization is similar to that of $0.14 \text{ emu}/\text{g}$ found in BFO grown using wet chemical method [40]. We predict no net magnetization for BFO grown in reducing conditions which is consistent with reduced magnetization in bulk ceramics samples grown using solid state reaction and sintered in vacuum or Ar or N[41]. Overall, bulk samples grown using various techniques do not show sizable magnetization, which is in agreement with our defect calculations. Other possibility of inducing ferromagnetism such as defect induced non-collinearity changing magnetic ordering of the Fe sub lattice, defect pairing and clustering, even though not considered in our calculation, can be expected to be small given dilute concentration of defects and large Néel temperature of 643 K in BFO. We further note that the long-wavelength spin density wave generated by spin canting out of the rotation plane of the antiferromagnetic cycloidal order, as seen in neutron scattering, also results in a small average local magnetization of about $0.06 \mu_B$ per Fe atom. [36] This effect is, however, not considered within our model.

Surprisingly, some thin-film samples have shown a large magnetization up to $0.5 \mu_B/\text{Fe}$ [36]. The effects of strain and/or interfaces have been put forward to explain this phenomenon[68]. We point out that thin-film growth is guided by complicated dynamic processes rather than the thermodynamic equilibrium which may contribute to the differences between bulk and thin film samples as well as that between thin films grown at different conditions. Given the stability of BFO being in a rather narrow window on the stability diagram (Fig. 1), film growth may be accompanied by the formation of second phases which may introduce magnetism in the system. Thorough structural characterization is critical to avoid these artifacts in experiments. Further,

the dependence of magnetization on film thickness [3,69] points towards the role of strain. In particular, tensile strain would decrease the energy of formation of V_{Bi} and V_{Fe} and produce large number of defects. However, the large magnetization of $\sim 0.5 \mu_{\text{B}}/\text{Fe}$ requires about 5% V_{Bi} or 1% V_{Fe} with respect to the total number of sites. In case of Fe vacancies there are further constraints that they have to be formed entirely in the ferromagnetically aligned planes, which seem to be unlikely. In any case, such high vacancy concentration should however be detectable in the experiments.

IV. CONCLUSIONS

We have investigated energetics of the intrinsic defects in bulk multiferroic BFO. We demonstrated that cation vacancies are dominant defects when the sample is grown under oxidizing conditions with no barrier for p-type doping or moving the Fermi level well below the VBM by applying external field. Only when the Fermi level lies well below VBM oxygen vacancies start appearing in comparable amount with cation vacancies. The number of oxygen vacancies has slight edge over the cation vacancies for the compound grown at reducing conditions, however overall concentration of either defect remains very small rendering a compound insulating. Oxygen vacancy is found to create a deep defect level that traps holes rather than generate electrons, whereas the cation vacancies are rather shallow and generate holes.

We find that the charge neutral Bi vacancies introduce an unpaired electron that couples with the Fe-3d electron changing its local moment and resulting in the net magnetization. Each Bi vacancy, when the Fermi level is close to VBM as in the oxidizing conditions, produces the

magnetic moment of $\sim 1\mu_B/\text{vacancy}$, whereas Fe vacancy produces the magnetic moment of $\sim 5\mu_B/\text{vacancy}$. The magnetic moments due to Bi vacancies are aligned ferromagnetically and thus contribute to the net magnetization, whereas the magnetic moments due to Fe vacancies may be aligned both ferromagnetically and antiferromagnetically and on average do not contribute to the net magnetization. Oxygen vacancies do not introduce any magnetism in either growth conditions. Due to point defects, BFO grown under the oxidizing conditions and high temperature may show small magnetization of $\sim 2 \text{ emu/cm}^3$, whereas BFO grown in reducing conditions is predicted to show no magnetization, due to relatively small number of defects. Thin film BFO, which are usually strained, in principle can have large number of cation vacancies due to the vacancy formation energy decreasing with the elongating bond especially due to the tensile strain. This would affect the stoichiometry of the compound due to Bi and Fe vacancies. However, producing large magnetization of about 70 emu/cm^3 ($\sim 0.5 \mu_B/\text{Fe}$) seen in some experiments requires a concentration of the Bi point defects ($\sim 5\%$). Such a sizable concentration of defects could be detected experimentally.

ACKNOWLEDGMENTS

This work was supported by the National Science Foundation (Grants Nos. EPS-1010674 and DMR-0906443). Computations were performed utilizing the Holland Computing Center of the University of Nebraska.

- [1] G.A Smolenskii and I. E. Chupis, Sov. Phys. Usp. **25**, 475-493 (1982).
- [2] Hans Schmid, Ferroelectrics **162**, 317-338 (1994).

- [3] J Wang, J B Neaton, H Zheng, V Nagarajan, S B Ogale, B Liu, D Viehland, V Vaithyanathan, D G Schlom, U V Waghmare, N A Spaldin, K M Rabe, M Wuttig, and R Ramesh, *Science* **299**, 1719-22 (2003).
- [4] Manfred Fiebig, *J. Phys. D* **38**, R123-R152 (2005).
- [5] Nicola A Spaldin and Manfred Fiebig, *Science* **309**, 391-2 (2005).
- [6] W Eerenstein, N D Mathur, and J F Scott, *Nature* **442**, 759-65 (2006).
- [7] Sang-Wook Cheong and Maxim Mostovoy, *Nat. Mater.* **6**, 13-20 (2007).
- [8] R Ramesh and Nicola A Spaldin, *Nat. Mater.* **6**, 21-9 (2007).
- [9] L W Martin, S P Crane, Y-H Chu, M B Holcomb, M Gajek, M Huijben, C-H Yang, N Balke, and R Ramesh, *J. Phys. Condens. Matter* **20**, 434220 (2008).
- [10] Daniel Khomskii, *Physics* **2**, 20 (2009).
- [11] K.F. Wang, J.-M. Liu, and Z.F. Ren, *Adv. Phys.* **58**, 321-448 (2009).
- [12] J P Velev, S S Jaswal, and E Y Tsymbal, *Phil. Trans. Royal Society A* **369**, 3069-97 (2011).
- [13] Jing Ma, Jiamian Hu, Zheng Li, and Ce-Wen Nan, *Advanced Materials (Deerfield Beach, Fla.)* **23**, 1062-87 (2011).
- [14] T Kimura, T Goto, H Shintani, K Ishizaka, T Arima, and Y Tokura, *Nature* **426**, 55-8 (2003).
- [15] Thomas Lottermoser, Thomas Lonkai, Uwe Amann, Dietmar Hohlwein, Jörg Ihringer, and Manfred Fiebig, *Nature* **430**, 541-4 (2004).
- [16] Craig Fennie and Karin Rabe, *Phys. Rev. B* **68**, 184111 (2003).
- [17] Ying-Hao Chu, Lane W. Martin, Mikel B. Holcomb, and Ramamoorthy Ramesh, *Mater. Today* **10**, 16-23 (2007).
- [18] H. Jang, S. Baek, D. Ortiz, C. Folkman, R. Das, Y. Chu, P. Shafer, J. Zhang, S. Choudhury, V. Vaithyanathan, Y. Chen, D. Felker, M. Biegalski, M. Rzchowski, X. Pan, D. Schlom, L. Chen, R. Ramesh, and C. Eom, *Phys. Rev. Lett.* **101**, 107602 (2008).
- [19] T Zhao, A Scholl, F Zavaliche, K Lee, M Barry, A Doran, M P Cruz, Y H Chu, C Ederer, N A Spaldin, R R Das, D M Kim, S H Baek, C B Eom, and R Ramesh, *Nat. Mater.* **5**, 823-9 (2006).

- [20] P Fischer, M Polomska, I Sosnowska, and M Szymanski, *J. Phys. C: Solid State Phys.* **13**, 1931-1940 (1980).
- [21] G. A. Smolenskii, V. Isupov, A. Agranovskaya, and N. Kranik, *Sov. Phys.-Solid State* **2**, 2651-2654 (1961).
- [22] J. Neaton, C. Ederer, U. Waghmare, N. Spaldin, and K. Rabe, *Phys. Rev. B* **71**, 014113 (2005).
- [23] P. Ravindran, R. Vidya, A. Kjekshus, H. Fjellvåg, and O. Eriksson, *Phys. Rev. B* **74**, 224412 (2006).
- [24] Claude Ederer and Nicola Spaldin, *Phys. Rev. Lett.* **95**, (2005).
- [25] J. Zhang, Q. He, M. Trassin, W. Luo, D. Yi, M. Rossell, P. Yu, L. You, C. Wang, C. Kuo, J. Heron, Z. Hu, R. Zeches, H. Lin, A. Tanaka, C. Chen, L. Tjeng, Y.-H. Chu, and R. Ramesh, *Phys. Rev. Lett.* **107**, 094115 (2011).
- [26] A. K. Pradhan, Kai Zhang, D. Hunter, J. B. Dadson, G. B. Loutts, P. Bhattacharya, R. Katiyar, Jun Zhang, D. J. Sellmyer, U. N. Roy, Y. Cui, and A. Burger, *J. Appl. Phys.* **97**, 093903 (2005).
- [27] Y P Wang, G L Yuan, X Y Chen, J-M Liu, and Z G Liu, *J. Phys. D* **39**, 2019-2023 (2006).
- [28] J Teague, *Solid State Commun.* **8**, 1073-1074 (1970).
- [29] C Michel, *Solid State Commun.* **7**, 701-704 (1969).
- [30] H. Béa, B. Dupé, S. Fusil, R. Mattana, E. Jacquet, B. Warot-Fonrose, F. Wilhelm, A. Rogalev, S. Petit, V. Cros, A. Anane, F. Petroff, K. Bouzehouane, G. Geneste, B. Dkhil, S. Lisenkov, I. Ponomareva, L. Bellaiche, M. Bibes, and A. Barthélémy, *Phys. Rev. Lett.* **102**, 217603 (2009).
- [31] Zuhuang Chen, Lu You, Chuanwei Huang, Yajun Qi, Junling Wang, Thirumany Sritharan, and Lang Chen, *Appl. Phys. Lett.* **96**, 252903 (2010).
- [32] R. Palai, R. Katiyar, H. Schmid, P. Tissot, S. Clark, J. Robertson, S. Redfern, G. Catalan, and J. Scott, *Phys. Rev. B* **77**, 014110 (2008).
- [33] Q He, Y-H Chu, J T Heron, S Y Yang, W I Liang, C Y Kuo, H J Lin, P Yu, C W Liang, R J Zeches, W C Kuo, J Y Juang, C T Chen, E Arenholz, A Scholl, and R Ramesh, *Nat. Commun.* **2**, 225 (2011).
- [34] S V Kiselev, R P Ozerov, and G S Zhdanov, *Sov. Phys. -Dokl.* **7**, 742 (1963).
- [35] Claude Ederer and Nicola Spaldin, *Phys. Rev. B* **71**, 224103 (2005).

- [36] J. Wang, A Scholl, H Zheng, S.B. Ogale, D Viehland, D. G. Schlom, N. A. Spaldin, K. M. Rabe, M. Wuttig, L. Mohaddes, J. Neaton, U. Wagemore, T. Zhao, R. Ramesh, W Eerenstein, F D Morrison, J Dho, M G Blamire, J F Scott, and N D Mathur, *Science* **307**, 1203b-1203b (2005).
- [37] Sheng Ju and Tian-Yi Cai, *Appl. Phys. Lett.* **95**, 231906 (2009).
- [38] S. J. Clark and J. Robertson, *Appl. Phys. Lett.* **94**, 022902 (2009).
- [39] Zhen Zhang, Ping Wu, Lang Chen, and Junling Wang, *Appl. Phys. Lett.* **96**, 232906 (2010).
- [40] Sverre M. Selbach, Mari-Ann Einarsrud, Thomas Tybell, and Tor Grande, *J. Am. Ceram. Soc.* **90**, 3430-3434 (2007).
- [41] Fengzhen Huang, Xiaomei Lu, Zhe Wang, Weiwei Lin, Yi Kan, Huifeng Bo, Wei Cai, and Jinsong Zhu, *Appl. Phys. A* **97**, 699-704 (2009).
- [42] G. Kresse, *Phys. Rev. B* **59**, 1758-1775 (1999).
- [43] G. Kresse, *Phys. Rev. B* **54**, 11169-11186 (1996).
- [44] P. E. Blöchl, *Phys. Rev. B* **50**, 17953-17979 (1994).
- [45] J. P. Perdew, *Phys. Rev. B* **23**, 5048-5079 (1981).
- [46] Vladimir I Anisimov, F Aryasetiawan, and A I Lichtenstein, *J. Phys. Condens. Matter* **9**, 767-808 (1997).
- [47] S. L. Dudarev, S. Y. Savrasov, C. J. Humphreys, and A. P. Sutton, *Phys. Rev. B* **57**, 1505-1509 (1998).
- [48] Vladan Stevanovi, Xiuwen Zhang, Stephan Lany, and Alex Zunger, *Renewable Energy Submitted to Phys. Rev. B.* (2011).
- [49] Claude Ederer and Nicola Spaldin, *Phys. Rev. B* **71**, 060401(R) (2005).
- [50] Hendrik Monkhorst and James Pack, *Phys. Rev. B* **13**, 5188-5192 (1976).
- [51] M Leslie and N J Gillan, *J. Phys. C: Solid State Phys.* **18**, 973-982 (1985).
- [52] G. Makov and M. C. Payne, *Phys. Rev. B* **51**, 4014 (1995).
- [53] Stefano Baroni and Raffaele Resta, *Phys. Rev. B* **33**, 7017-7021 (1986).
- [54] Stephan Lany and Alex Zunger, *Phys. Rev. B* **78**, 235104 (2008).

- [55] Stephan Lany and Alex Zunger, *Modell. Simul. Mater. Sci. Eng.* **17**, 084002 (2009).
- [56] Stephan Lany and Alex Zunger, *Phys. Rev. Lett.* **106**, 069601 (2011).
- [57] Hannes Raebiger, Stephan Lany, and Alex Zunger, *Nature* **453**, 763-766 (2008).
- [58] Stephan Lany and Alex Zunger, *Phys. Rev. B* **80**, 085202 (2009).
- [59] Stephan Lany, *Phys. Rev. B* **78**, 245207 (2008).
- [60] Jorge Osorio-Guillen, Stephan Lany, Alex Zunger, and Jorge Osorio-Guillén, *Phys. Rev. Lett.* **100**, 036601-4 (2008).
- [61] Tula R. Paudel, Andriy Zakutayev, Stephan Lany, Mayeul D’Avezac, and Alex Zunger, *Adv. Funct. Mater.* **21**, n/a-n/a (2011).
- [62] Donald Wagman, *The NBS Tables of Chemical Thermodynamic Properties*: Selected Values for Inorganic and C1 and C2 Organic Substances in SI Units (American Chemical Society and the American Institute of Physics for the National Bureau of Standards, New York; Washington D.C., 1982).
- [63] J. F. Ihlefeld, N. J. Podraza, Z. K. Liu, R. C. Rai, X. Xu, T. Heeg, Y. B. Chen, J. Li, R. W. Collins, J. L. Musfeldt, X. Q. Pan, J. Schubert, R. Ramesh, and D. G. Schlom, *Appl. Phys. Lett.* **92**, 142908 (2008).
- [64] Ashish Garg, Steven Dunn, and Zoe H. Barber, *Integrated Ferroelectrics* **31**, 13-21 (2000).
- [65] Koushik Biswas and Stephan Lany, *Phys. Rev. B* **80**, 115206 (2009).
- [66] A.S. Poghossian, H.V. Abovian, P.B. Avakian, S.H. Mkrтчian, and V.M. Haroutunian, *Sensors and Actuators B: Chemical* **4**, 545-549 (1991).
- [67] Zhonghua Dai and Yukikuni Akishige, *J. Phys. D* **43**, 445403 (2010).
- [68] P. Yu, J.-S. Lee, S. Okamoto, M. Rossell, M. Huijben, C.-H. Yang, Q. He, J. Zhang, S. Yang, M. Lee, Q. Ramasse, R. Erni, Y.-H. Chu, D. Arena, C.-C. Kao, L. Martin, and R. Ramesh, *Phys. Rev. Lett.* **105**, 027201 (2010).
- [69] Yao Wang, Qing-hui Jiang, Hong-cai He, and Ce-Wen Nan, *Appl. Phys. Lett.* **88**, 142503 (2006).

FIGURE CAPTIONS:

Fig. 1: Stability regions of different compounds against Bi and Fe chemical potentials. The black and blue lines represent the stability transition lines between Fe_2O_3 and BFO and Bi_2O_3 and BFO respectively. The stability region of BFO is indicated in the green. The chemical potential iso-line labeled O_2 molecule corresponds to the most oxidizing condition ($\Delta\mu_{\text{O}} = 0$), which reduces while going towards the origin. Other phases such as $\text{Bi}_2\text{Fe}_4\text{O}_9$, Fe_3O_4 and FeO do not change the BFO region of stability.

Fig. 2: Enthalpy of formation of various intrinsic defects as a function of the Fermi energy in the band gap of BFO for oxygen rich (a) and oxygen poor (b) conditions. Straight lines represent charge states of the defect and break points shown by solid circles represent the charge transition energy. Only the most stable charge state of a defect at a given Fermi energy is shown. E_V and E_C denote positions of the valence band maximum and the conduction band minimum, respectively. The shaded regions show the accessible range of the Fermi energy.

Fig. 3 : The relative number of defects as a function of the oxygen chemical potential at ambient pressure and 723°C .

Fig. 4 : Calculated density of states (DOS) as a function of energy for bulk BiFeO_3 containing charge-neutral Bi vacancies (a) and the coupling mechanism between the Bi vacancy and host Fe atom in BiFeO_3 (b). The top panel in (a) shows the total DOS and the bottom panel shows the Fe-3d partial DOS. An arrow indicates a-like vacancy state.

Fig. 5: Calculated density of states (DOS) as a function of energy for bulk BiFeO_3 containing O vacancies (a) and the coupling mechanism between the O vacancy and the host Fe atom in

BiFeO₃ (b). The top panel in (a) shows the total density of states (DOS) and the bottom panel shows sum of Fe-d partial DOS. An arrow indicates denotes a-like vacancy state.

FIGURES:

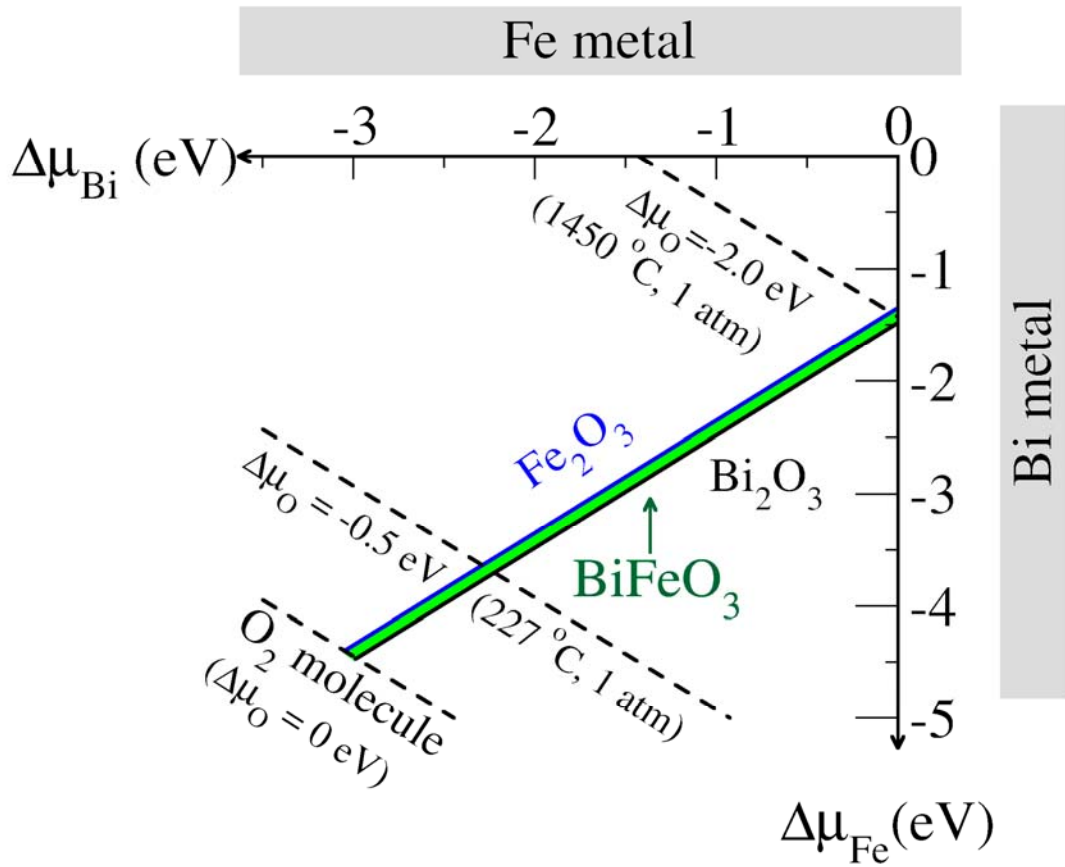


Fig.1

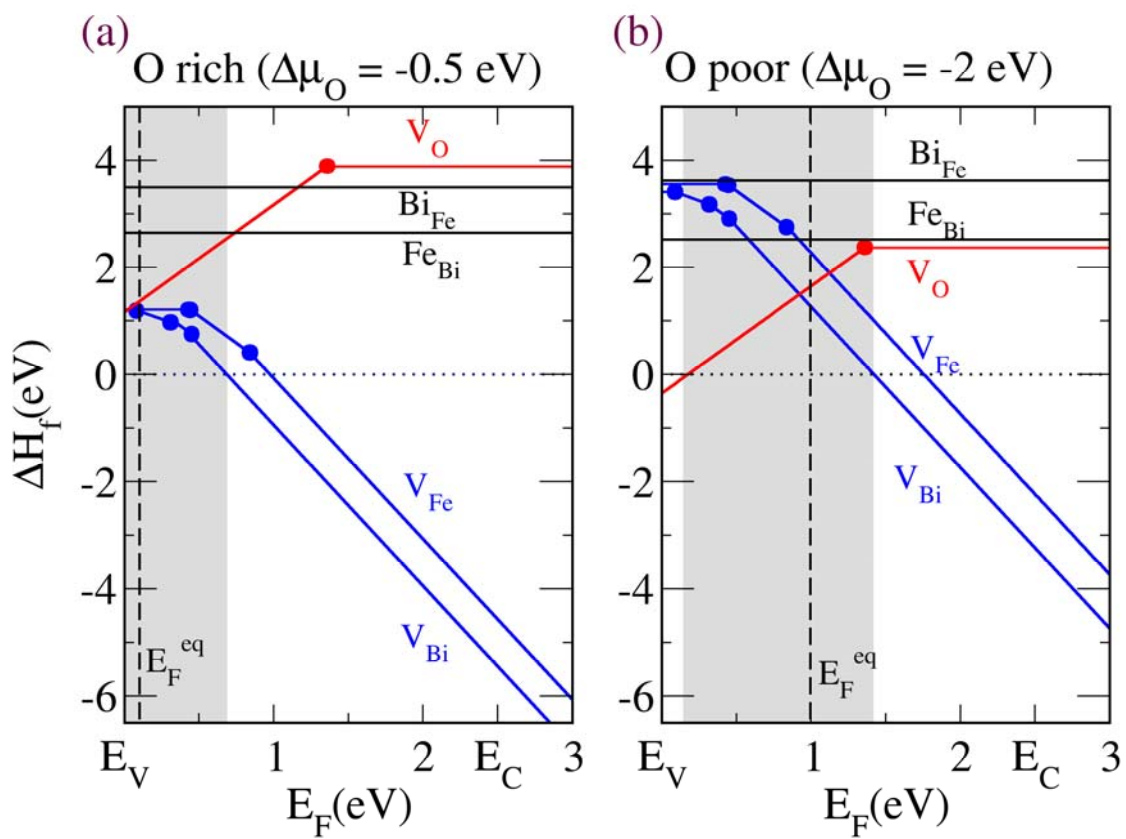


Fig. 2

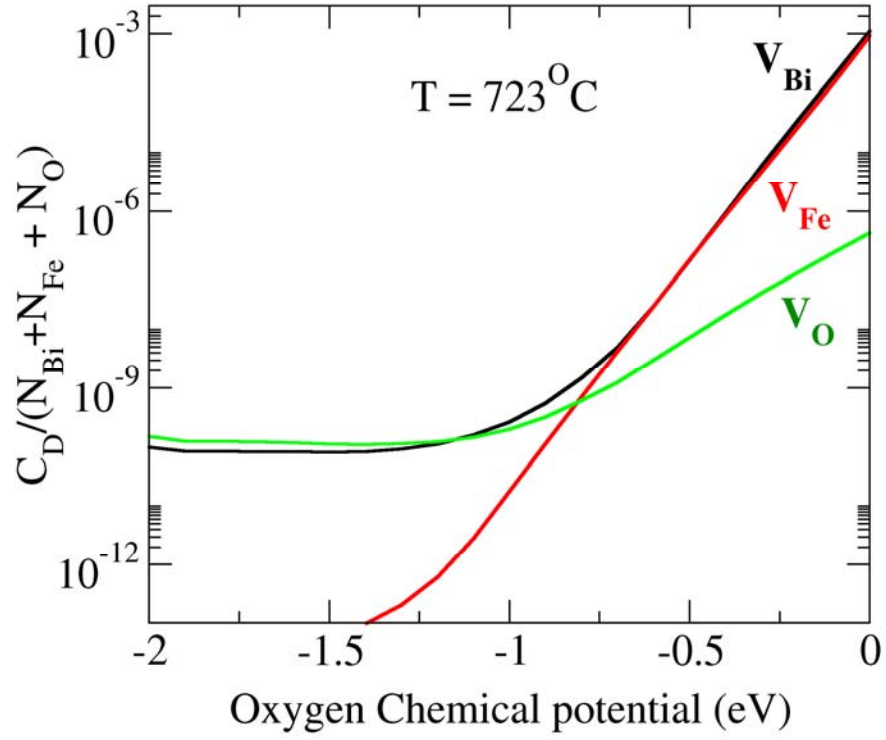


Fig. 3

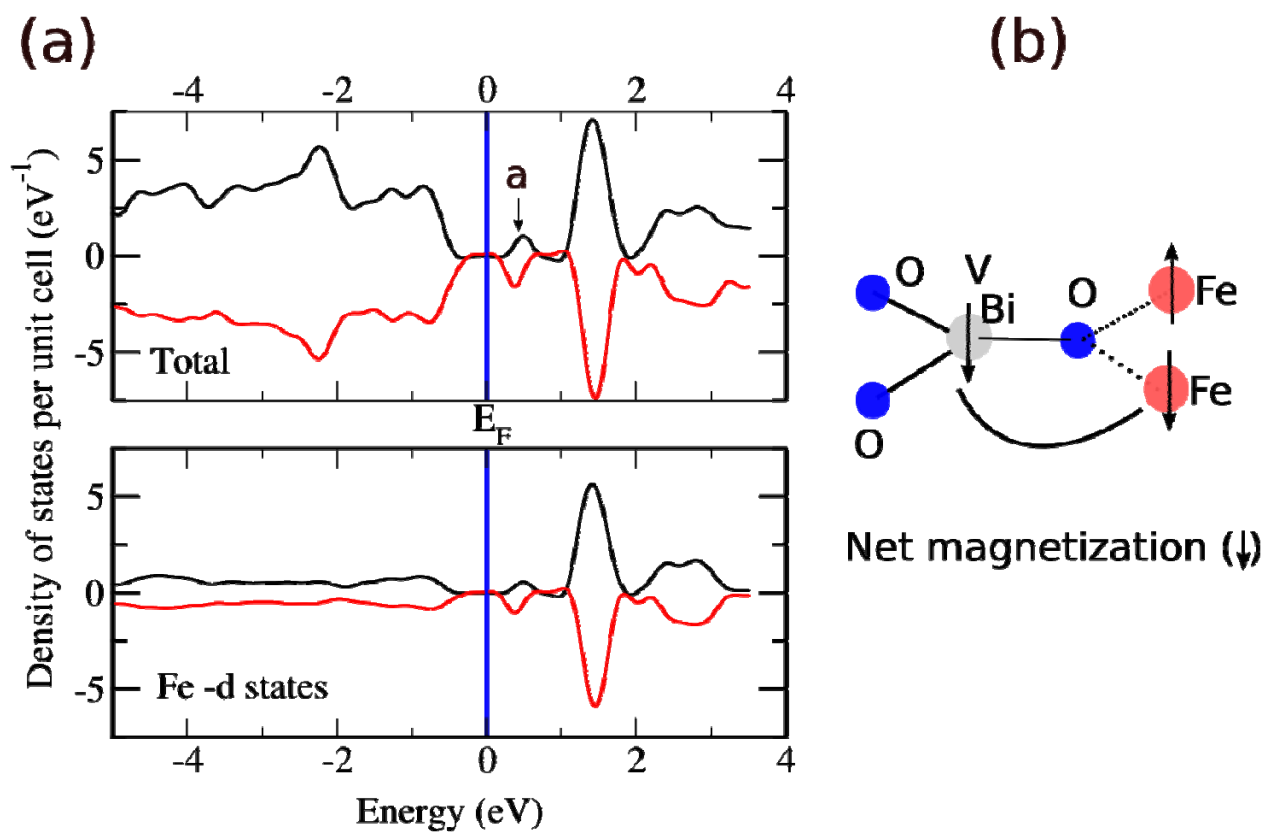


Fig.4

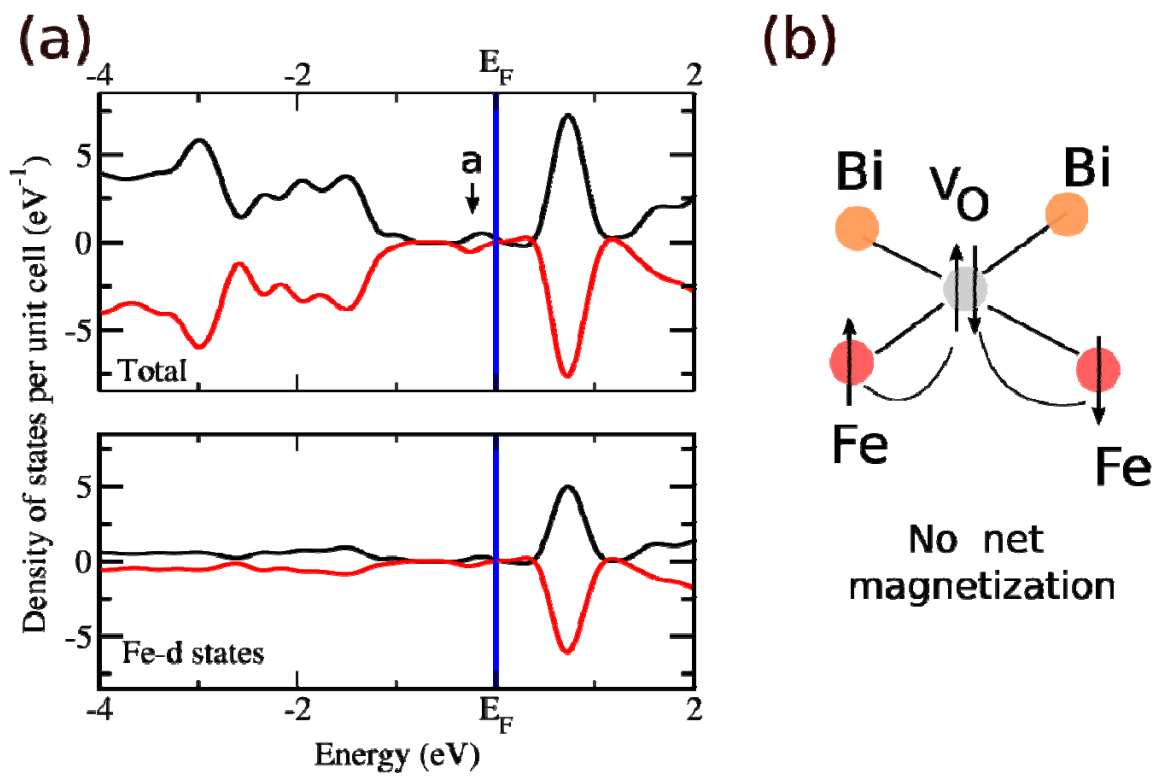


Fig. 5